Analysis of a Direct-Drive Ignition Capsule Designed for the National Ignition Facility

Introduction

One of the primary missions of the National Ignition Facility[1] (NIF) is to achieve fusion ignition and moderate gain by means of inertial confinement fusion (ICF). A typical ICF experiment involves the implosion of a small spherical capsule containing deuterium–tritium (DT) fuel using high-power laser light. The energy is absorbed in a thin, outer region of the capsule, which quickly heats and ablates, expanding outward and accelerating the remainder of the capsule inward, compressing the contained DT fuel to ignition conditions. The implosion can be tailored to give a number of assembled fuel configurations of which the most energy efficient[2] is isobaric with a central high-temperature hot spot surrounding a low-temperature main fuel layer. The central hot spot initiates the fusion reaction, which leads to a burn wave propagating into the main fuel layer. For direct-drive target designs two main effects can prevent the correct assembly of the fuel: (1) preheat of the fuel[3] and (2) hydrodynamic instabilities of the imploding shell.[2,4–6]

Hydrodynamic instabilities, and their effects on imploding ICF capsules, have been the subject of extensive studies in the past.[2,6–11] Nonuniformities in the applied drive, coupled with imperfections at the target surface, seed Rayleigh–Taylor (RT) unstable growth at the ablation front. In addition, rarefaction waves generated at the perturbed inner ice surface, due to the breakout of the first shock, return to the ablation region and contribute to the instability there.[12–14] These perturbations feed through the shell and couple with the existing perturbations on the inner ice surface. This combination serves as the seed for RT growth at the ice/vapor interface when the ice layer begins to decelerate around the hot spot.

A good understanding of how the unstable growth of perturbations affects target performance (ignition and gain) is required to guide the development of the laser and target systems' specifications. Of specific importance is the designation of parameters dealing with the allowable levels of roughness at both the outer and inner surfaces of the capsule, the allowable limit on laser power imbalance and beam mistiming, and the amount of bandwidth requirements for single-beam uniformity. A consistent scaling that includes the net effect of all of these mechanisms acting together is developed. Such a "nonuniformity budget" adds flexibility in the design of the laser and target systems, allowing trade-offs to be made among the four sources of nonuniformity.

This article will first examine briefly the current direct-drive point design[3,6,15] for the NIF. Using one-dimensional 1-D *LILAC*[16] results, we show that the capsule design is robust. Next we examine the scaling of target gain in terms of a spectral ensemble of the rms surface roughness of the inner ice surface ($\bar{\sigma}$) at the end of the acceleration phase of the implosion. The scaling of gain with $\bar{\sigma}$, developed using the results of many two-dimensional (2-D) *ORCHID*[17] simulations, allows for the definition of a global nonuniformity budget that can ascertain the relative significance of the different nonuniformity sources in reducing capsule performance. In addition, the modeling of each of the four perturbation mechanisms is discussed. Overall target gain results are evaluated, and the scaling of the physical specification being modeled (e.g., outer-surface roughness) with $\bar{\sigma}$ is established. We also discuss the physical mechanisms that determine why target gain scales with $\bar{\sigma}$. Finally, we construct an overall nonuniformity budget for NIF systems, using the combined effects of each of the four perturbation mechanisms.

Point Direct-Drive Target Design for NIF

The base-line direct-drive designs for NIF employ a solid (cryogenic) DT-shell target with a thin polymer ablator (required to fabricate the cryogenic shell) surrounding the DT-ice shell.[3,15] The designs use shock preheat to control the isentrope of the ablation surface and the fuel. Variation in the isentrope ($\alpha = 1$ to 4, where α is the ratio of the fuel pressure to the Fermi-degenerate pressure) is achieved by varying the incident laser pulse shape. Based on the results of current OMEGA experiments and theoretical calculations of these NIF designs, we have selected the 1.5-MJ, $\alpha = 3$ design to be the point design for further study.

The point design has been shown[3] to be robust to several design uncertainties including control of laser pulse shape, material equation-of-state modeling, operating temperature, and the effects of hot electrons produced by laser–plasma instabilities (LPI). Figure 84.7(a) shows the target specification; Fig. 84.7(b) shows the pulse shape for this design. The DT-ice thickness and adiabat of the implosion determine the intensity and duration of the foot. In this design, the foot is 4.25 ns long at a power of 10 TW. This region launches a 10-Mbar shock through the DT ice. At the time of shock breakout at the rear surface of the DT ice, the pulse ramps up to the drive region, which lasts for 2.5 ns at a power of 450 TW. This rapid rise in intensity generates pressures of approximately 80 Mbar and thus accelerates the DT ice inward. The $\alpha = 3$ design is predicted, by 1-D calculations, to have a gain of 45, a neutron-averaged ion temperature of 30 keV, and a peak fuel ρR = 1.3 g/cm^2. The peak in-flight aspect ratio (IFAR) of this design is 60, and the hot-spot convergence ratio is 29.

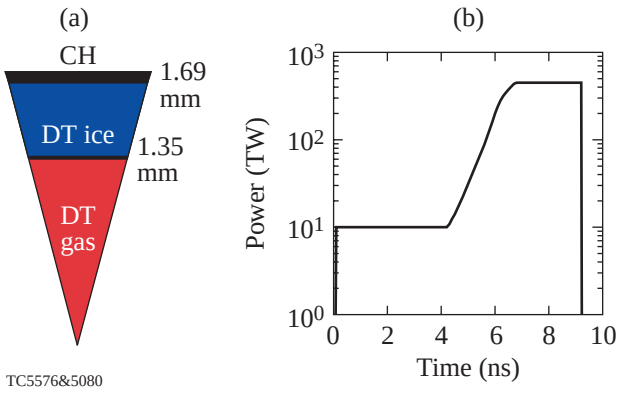

Figure 84.7
The base-line, $\alpha = 3$, "all-DT," 1.5-MJ target design. (a) The target specification and (b) the pulse shape.

Modeling Sources of Nonuniformities

During the foot pulse, the laser intensity is constant and the ablation front travels at constant velocity. While no RT unstable growth is present during this time, perturbations could still grow due to the presence of power imbalance, outer-surface roughness [Ritchmyer–Meshkov (RM)-like instability][18] and laser nonuniformity (laser imprint).[18–20] Later, when the laser intensity ramps up to drive conditions, the ablation front starts to accelerate, producing conditions for RT growth that amplify the target nonuniformities seeded during the foot pulse. Establishing the relative importance of each source of nonuniformity requires that a time in the implosion at which all sources complete their contribution to the total nonuniformity be identified. Since perturbations due to power imbalance grow through the whole laser pulse, laser imprint and RM growth occur only during the foot pulse, and the feedout brings perturbation to the unstable ablation front during the main pulse, the best choice is at the end of the acceleration phase. At this time the ice/vapor surface perturbations decouple from the now-stable ablation surface. To construct a scaling of gain versus mode spectrum at the ice/vapor surface ($\bar{\sigma}$), 2-D *ORCHID* burn calculations were compiled to examine the effects of various, initially applied, ice/vapor-interface perturbation spectra ($\ell = 2$–50) on target gain. It was found that the target gain can be well represented in terms of an effective nonuniformity ($\bar{\sigma}$) that gives a reduced weight to the low-order modes ($\ell < 10$):

$$\bar{\sigma} = \sqrt{0.06\,\sigma^2_{\ell<10} + \sigma^2_{\ell>9}}\,, \qquad (1)$$

where $\sigma^2_{\ell<10}$ is the sum-in-quadrature of all modes of nonuniformity with $\ell < 10$ and $\sigma^2_{\ell>9}$ is the corresponding sum for $\ell > 9$. Results of this scaling, shown in Fig. 84.8, indicate that the gain threshold for point design occurs at a value of $\bar{\sigma} = 2.5$.

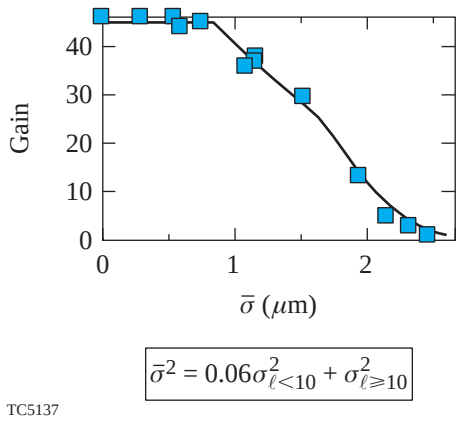

Figure 84.8
The reduction in target gain is drawn as a function of an ensemble of modal amplitudes taken at the ice/vapor interface at the end of the acceleration phase of the implosion.

From Eq. (1), it can be seen that the high-order modes can be significantly more damaging to capsule gain than that due to the low-order modes. The small $\bar{\sigma}$ weighting of the low-order modes is just a reflection of two effects. First, as has been shown in several single-mode studies,[21,22] capsule gain is far more tolerant of levels of low-order modes than the high-order modes. Secondly, during the deceleration phase of the implosion, low-order modes experience less growth than the high

ℓ modes.[23,24] During the acceleration phase at the ablation front, the development of the high-order modes, seeded from the laser imprint, feedout from the inner ice surface, and the outer-surface roughness, is critical in determining the integrity and survivability of the shell. Due to lateral smoothing, however, the high-order modes do not feed through efficiently to the inner ice surface. The result is that the low-order modes tend to dominate the inner ice roughness at the end of the acceleration phase.[8]

These results help construct 2-D simulations of the four main perturbation mechanisms: laser imprint, power imbalance, and inner- and outer-target-surface roughness. Each of the four mechanisms was studied independently to evaluate the sensitivity of gain to variations in the laser and target system specifications. Applying the $\bar{\sigma}$ scaling to the results allows a nonuniformity budget for NIF to be determined. By establishing a global budget in terms of $\bar{\sigma}$, it is possible to evaluate the contribution of each source to the problem as a whole, providing insight into the mission-critical nonuniformities, and giving direction for trade-offs between the various sources of nonuniformity. A discussion of the modeling, sample numerical results, and how gain scales with $\bar{\sigma}$ for each perturbation mechanism follows.

1. Power Balance

The term "power balance" can be applied to a wide range of temporal, beam-to-beam intensity differences, arising from laser amplifier saturation, beam mistiming, variations in frequency conversion (angular or polarization tuning), and/or the transport of the UV energy to the target. The effects of power imbalance on the applied irradiation are modeled by determining the on-target power variations between the beams due to their propagation through the laser system. Each beam develops a unique temporal power history, which is used to calculate the irradiation nonuniformity on-target over the entire implosion. Many NIF laser power histories were calculated by Jones[25] and supplied to the authors.

Further modeling uses 1-D *LILAC* density and temperature profiles and a 2-D laser absorption routine from *ORCHID* to determine the absorbed energy at the critical surface for a single beam. This absorption profile is scaled for each beam and, using the orientation of the beam, mapped onto a sphere representing the critical surface of the target. All 192 beamlets of the NIF system are mapped to 48 unique positions on the sphere. The resulting spherical intensity distributions are then decomposed for each time and used as input to 2-D *ORCHID* simulations.

Two series of 2-D *ORCHID* runs were completed using each of the NIF power histories. The first series used the calculated power imbalance as supplied by Jones,[25] while the second series artificially doubled the power imbalance to determine ignition thresholds. In addition, further runs were compiled to assess the effects of beam mistiming for each series. A contour plot of mass density at stagnation from a typical power imbalance *ORCHID* simulation, illustrated in Fig. 84.9, clearly shows the presence of low-order modes distorting the core region. Compiling the results of these simulations, shown in Fig. 84.10, illustrates the degradation of yield with increasing on-target nonuniformities and beam-to-beam mistiming. The target gain is shown plotted against the on-target rms perturbation. The base-line NIF requirements for power balance and beam mistiming have been given as 8% rms beam-to-beam and 30-ps rms beam-to-beam, respectively.[26] The reduction in gain for these requirements is low (~10%). The results are also plotted against their calculated values of $\bar{\sigma}$ in Fig. 84.10(b). A $\bar{\sigma}$ value of ~0.85 corresponds to the NIF requirements for power imbalance.

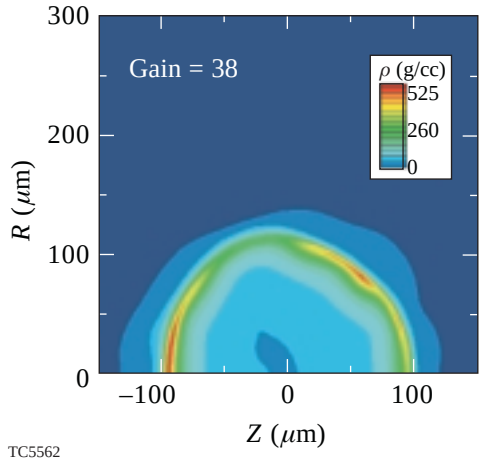

Figure 84.9
Core disruption due to NIF specifications of power imbalance and beam mistiming is dominated by low-order modes but has little effect on target gain.

2. Ice/Vapor Surface Roughness

Since there is uncertainty in the initial ice spectrum, 2-D *ORCHID* simulations were completed assuming an initial prescription for the spectral behavior and amplitude of the roughness of the form $a = a_0/\ell^{\beta}$. Variations in β and total σ_{rms} were examined from 0 to 1.5 and 0.5 to 12 μm, respectively. These simulations assumed smooth outer surfaces and perfect laser illumination. Figure 84.11 shows an example where the initial surface roughness of the ice/vapor interface was 3.8-μm rms (2.0-μm rms summed over modes 10 to 50) with $\beta = 0.75$.

Figure 84.11(a) illustrates the density contours of the imploding shell at stagnation. Perturbations at the ablation front are clearly visible. Comparing the roughness spectrum ice/vapor interface at the end of the acceleration phase with that of the initial spectrum, illustrated in Fig. 84.11(b), it can be seen to have increased in magnitude and steepened to a higher order of β. These results are typical of the behavior of the inner ice perturbations. They can be attributed to the unique process of feeding out to the ablation surface, undergoing RT growth, and then feeding back into the original surface. The low modes dominate with the high modes being filtered by lateral smoothing while traversing the ice layer.

The results from this series of 2-D *ORCHID* runs are compiled in Fig. 84.12. In Fig. 84.12(a), the behavior of target gain is drawn as a function of the rms of just the low-order modes (ℓ = 2–10). These curves indicate that while the low-order modes are dominant, the high-order modes, as the applied spectra flatten, cannot be ignored. However, Fig. 84.12(b) shows the gain can be well represented by the behavior of $\bar{\sigma}$, regardless of the applied spectrum.

3. Outer-Surface Roughness

The direct-drive point design has traditionally been called the "all-DT" design, which is a misnomer. The DT-ice capsule

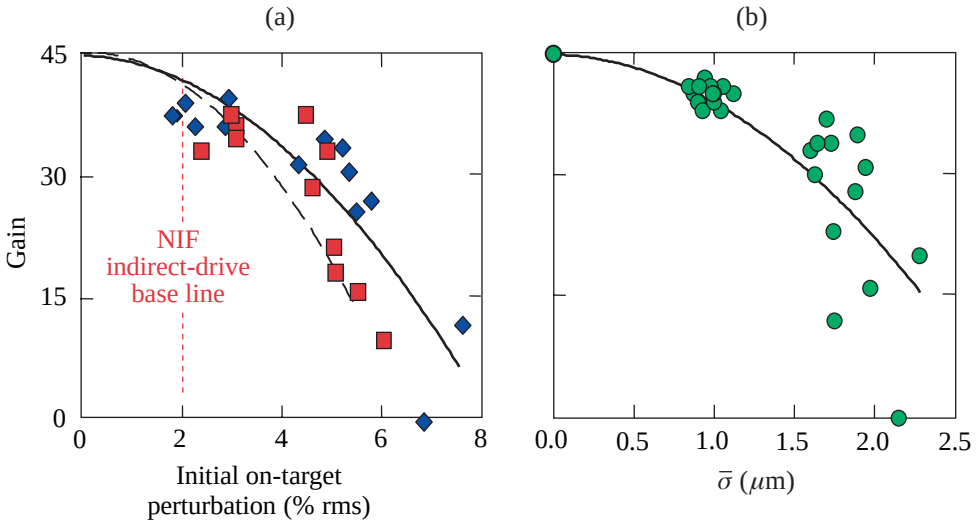

Figure 84.10
NIF laser power histories have been used to validate the NIF base-line power imbalance specifications. (a) Calculated target gain is drawn as a function of the on-target rms perturbation for beams with perfect timing (◆) and beams with a 30-ps rms (beam-to-beam) mistiming (■). (b) Calculated target gain is shown to scale well with $\bar{\sigma}$.

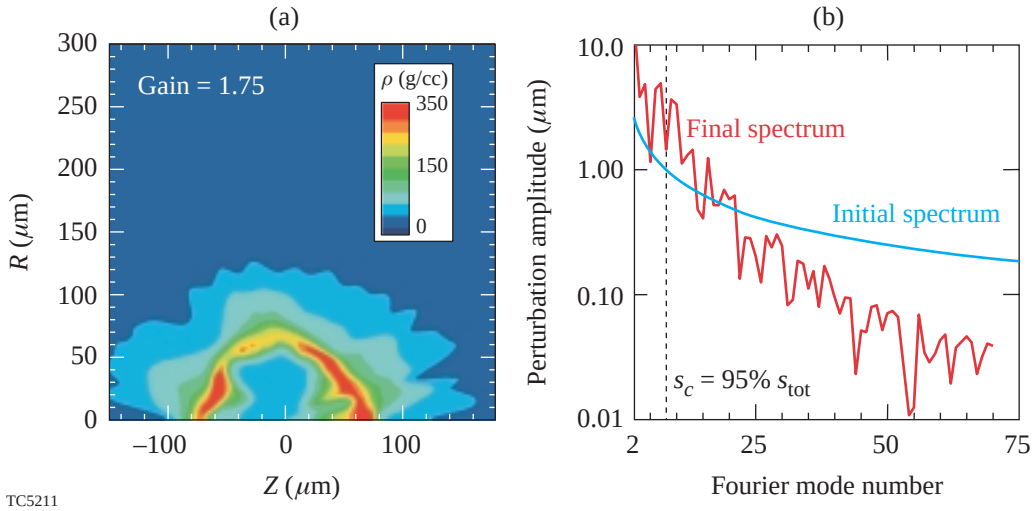

Figure 84.11
Results from *ORCHID* simulation indicate target gain depends strongly on the development of the low-order modes. (a) Density contours drawn at the time of stagnation. Note that the gain for this target was reduced from 45 to ~2. (b) Spectra of ice/vapor interface at the beginning and end of the implosion. Note the concentration of power in the low-order modes at stagnation.

is actually fabricated within a thin (1- to 2-μm) plastic microballoon, which serves, albeit for a short time, as an ablator. The density mismatch at the CH/DT interface can lead to additional perturbation growth at the ablation front. Indeed, when the shock reaches the interface, it produces a transmitted shock into the DT and a reflected rarefaction wave that moves back out toward the ablation surface. After the rarefaction wave breaks out at the ablation front, the latter starts to accelerate at $a \sim \left(p^{\mathrm{CH}} - p^{\mathrm{DT}}\right)/(\rho d)$, where ρ and d are initial density and thickness of CH layer, and p^{CH} and p^{DT} are the post-shock pressures in CH and DT, respectively. The acceleration occurs for a time interval $\Delta t_{\mathrm{acc}} \sim d/c_s$ (until the compression wave is generated at the ablation front), where c_s is the sound speed of the compressed ablator material. During the acceleration, the ablation surface is RT unstable, and perturbations in the front grow by a factor $\exp\left(\sqrt{ka\Delta t_{\mathrm{acc}}^2}\right) \sim \exp\left(\varepsilon\sqrt{kd}\right)$, where the coefficient ε depends on the shock strength. Furthermore, since the ablation front is rippled, the rarefaction wave breaks out first at the front's valleys and then at the peaks. Thus, there is a delay Δt_{rw} between accelerating the peaks and valleys of the ablation front. This delay creates an additional velocity perturbation $\delta v = a\Delta t_{\mathrm{rw}}$. The RT growth and δv increase the kinetic energy of the front ripple, leading to a higher perturbation amplitude. Since the RT growth factor increases with the ablator thickness d, minimizing the perturbation growth during the foot pulse requires the minimum thickness of the ablator layer.

Modeling the effects of these perturbations on indirect-drive target performance[7–10] has led to an outer-surface spectrum that is considered by target fabrication groups to be the "NIF standard." A series of 2-D *ORCHID* simulations were compiled using the NIF standard as a base-line level of surface roughness (σ = ~115 nm). The power spectrum of the nonuniformity was then doubled and quadrupled to determine the resultant ice/vapor surface distortion at the end of the acceleration phase. As can be seen in Fig. 84.13, the effect of these

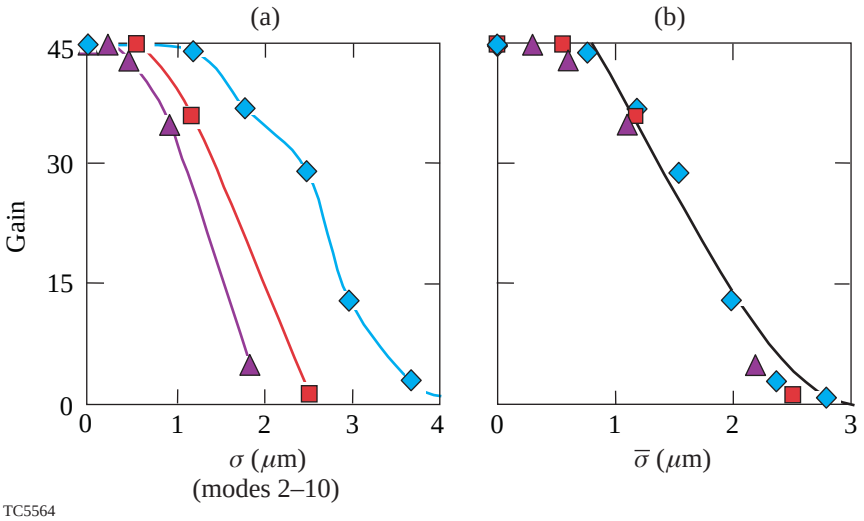

Figure 84.12
Results from *ORCHID* simulation of inner-ice-surface roughness indicate that high-order modes contribute to the reduction of capsule gain. Mode amplitudes obey $a = a_0/\ell^{\beta}$, $\beta = 0.00$ (▲), 0.75 (■), and 1.50 (◆). (a) Calculated target gain is drawn as a function of the initial rms finish of the ice layer in modes 2–10. (b) Calculated target gain is now drawn as a function of the calculated values of $\bar{\sigma}$.

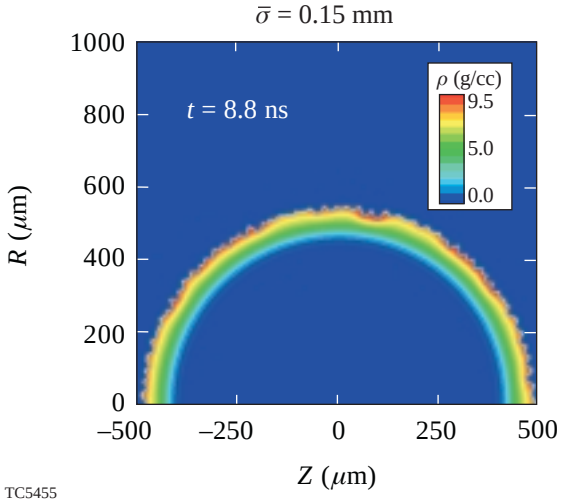

Figure 84.13
ORCHID simulations, using twice the NIF standard surface roughness (230 nm), reveal no significant disruption of the ice/vapor interface at the end of the acceleration phase of the implosion.

levels of surface roughness on the ice/vapor interface has been minimal. While the density contours show a ~4-μm perturbation at the ablation surface, the inner-ice-surface layer shows no appreciable disruption. After analysis, the rms value of the resultant spectrum results in a value of $\bar{\sigma} \sim 0.15$. These results are consistent with Goncharov's analytic model[18,27] and indicate that the gain of the direct-drive point design is insensitive to outer-surface roughness below our calculations of ~250 nm. These results indicate that, if given the NIF standard roughness, the outer surface of the direct-drive point design will not contribute significantly to the global nonuniformity budget.

4. Laser Imprint

The last, and possibly most important, source of nonuniformity for the direct-drive point design is the imprinting of variations in the laser-beam profile onto the surface of the capsule. Our understanding of imprint is based on both theory[18,20] and experiment.[19,28] These studies have shown that, without any temporal smoothing of laser profiles, imprinted perturbations will lead to shell failure during the implosion. Smoothing of individual laser profiles is a major issue for direct drive. The direct-drive design for NIF includes the combined application of a distributed phase plate (DPP),[29,30] polarization smoothing,[31] and smoothing by spectral dispersion (SSD)[32] within each of its 192 beams.

In modeling the irradiation nonuniformity, the single-beam DPP spectrum[33] (modes 2 to 200) is modified for the 40-beam overlap and the use of polarization smoothing. The application of SSD produces statistically independent speckle patterns every $\Delta t = t_c$, where $t_c = 1/\left[\Delta\nu \sin\left(kn\delta/2\right)\right]$ is the correlation time ($\Delta\nu$ is the laser bandwidth, n is the number of color cycles, and δ is the speckle size, which is 7 μm for NIF). The NIF specification for smoothing has been given as 1-THz bandwidth and two color cycles. In the case of the constant-intensity foot pulse, this reduces the time-averaged laser nonuniformity by a factor $\sqrt{\left(t_c/\langle t\rangle\right)}$, where $\langle t\rangle$ is the averaging time. The longest wavelength that can be smoothed by SSD is determined by the maximum angular spread $\Delta\theta$ of the light propagating through the laser.[34] Using $\Delta\theta = 100$ μrad and a laser focal length $F = 700$ cm, SSD can smooth spherical-harmonic modes down to $\ell_{\text{cut}} = 15$. To model these intensity variations, a series of *ORCHID* simulations were compiled, randomly changing the sign of the individual laser mode amplitudes every $\Delta t = t_c$. The laser power histories for these runs were then averaged giving a smoothing rate similar to that of SSD, which was then applied to a single simulation.

Calculations for the effect of laser imprint have been performed to determine the ice/vapor distortion at the end of the acceleration phase of the implosion. Comparing the density contours of two separate implosions of the same shell, driven under different imprint scenarios, illustrates the need for this level of smoothing. The majority of *ORCHID* simulations below were performed with one color cycle to determine the minimal level of smoothing. Figure 84.14 shows the density contours for two implosions of the same shell using (a) no bandwidth and (b) 1-THz bandwidth (one color cycle). The calculated values of $\bar{\sigma}$, compiled from a series of *ORCHID* simulations, can be used to project the target gain as a function of applied bandwidth as shown in Fig. 84.15. From this graph it can be seen that deploying 1-THz bandwidth at one color cycle results in a 30% reduction in gain. For the same bandwidth higher uniformity can be achieved in the spectral range of interest by increasing the number of color cycles[31,35] (usually achieved by increasing the SSD modulator frequency). An additional *ORCHID* simulation, employing 1 THz and two

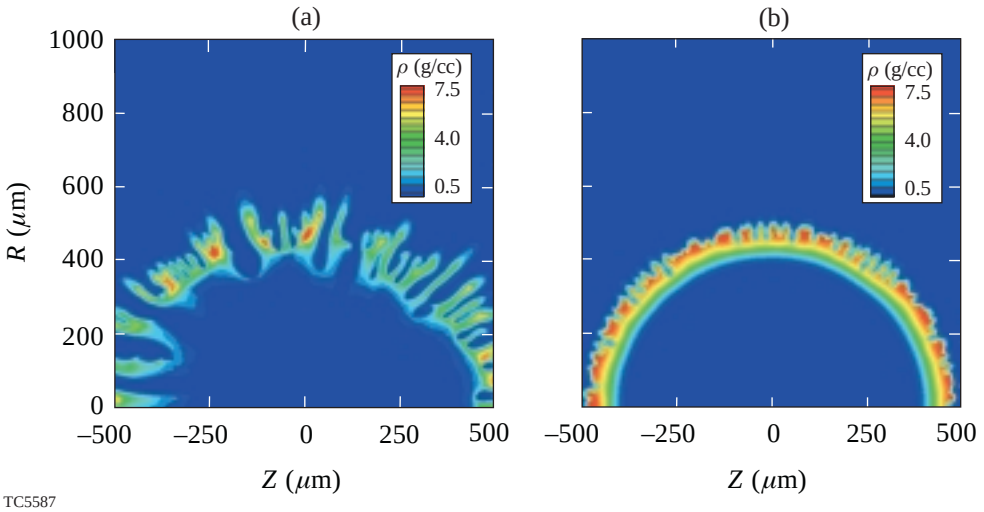

Figure 84.14
The need for high levels of bandwidth and multiple color cycles is evident when comparing density contours for two implosions of the same shell, applying (a) no bandwidth or (b) 1-THz bandwidth (one color cycle).

color cycles, was analyzed, and the result is plotted as the single annotated point in Fig. 84.15. It can be seen that either doubling the bandwidth or deploying two color cycles would recover almost the full design gain for the capsule. The NIF specifications, 1-THz bandwidth with two color cycles, correspond to a $\bar{\sigma}$ value of 1.0.

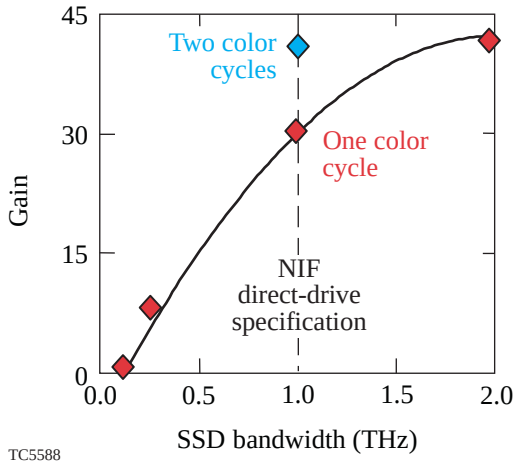

Figure 84.15
Projected target gain, using $\bar{\sigma}$ scaling, drawn as a function of the applied laser bandwidth for the direct-drive NIF point design capsule

Gain Reduction

There are three distinct regions in the behavior of the gain as a function of $\bar{\sigma}$. The first extends from $\bar{\sigma}$ equal to zero out to about to 1, the second from 1 out to about 2.5, and the third for $\bar{\sigma}$ above 2.5. While the first and third regions are easily explained by minimal effect of small perturbations on gain in the first region and total ignition failure in the third, a consistent argument to connect the two regions while explaining the middle ground can be found by examining the sequence of events leading to high gain in an unperturbed implosion.

It is well known that the main precursor to ignition is the incoming shell motion providing PdV work to the hot spot. As the shell moves in and heats the hot spot, it also provides the necessary ρR, enabling efficient absorption of α-particle energy.[2] The combination of these two must exceed any losses due to thermal conduction and radiation transport out of the hot spot. If done correctly, ignition occurs and a burn wave begins to move out into the cold fuel shell. It is at this point, however, that the disposition of the shell re-enters the problem. As the burn wave moves out into the ice layer, it exerts a tremendous pressure on the shell. In ICF targets it is typically the hydrodynamic expansion of the ignited fuel that quenches the burn.[23] If, however, the shell still retains some of its original radial kinetic energy, the inward momentum of the shell acts as a tamper to increase the ρR of the fuel while preventing the burn wave from decompressing the shell prematurely.

Levedahl and Lindl[36] have shown how excess kinetic energy in the shell, above that required for ignition, leads to a higher burn-up fraction. Their results show that the burn-up fraction can be drawn as a function of a dimensionless parameter that equals 1 for NIF capsules that marginally achieve ignition. As the retained kinetic energy in the shell is increased, the burn-up fraction climbs sharply until leveling off for kinetic energies in excess of 2 to 4 times the ignition energy. The sharp increase in burn-up fraction is referred to as the "ignition cliff" and indicates that NIF capsules need 1 to 2 times the kinetic energy above that which is required for ignition to achieve high gain. The ratio of excess radial kinetic energy to the maximum in-flight radial kinetic energy of the shell is referred to as "implosion margin" or simply "margin." To achieve burn-up fractions above 10% requires margins above 30%. The margin for the direct-drive point design is 40%, which results in a burn-up fraction of ~15%. The point design delivers a gain of 45, which is directly related to the burn-up fraction. The gain threshold ($G = 1$) for this target is roughly 1.1 times the ignition energy or a margin of roughly 10%.

Margin is directly related to the hydrodynamic stagnation of the incoming shell, and typically only the pressure associated with an ignited burn wave can force the shell off its normal trajectory. If, for a moment, we examine the point design with thermonuclear burn turned off, we can see, as shown in Fig. 84.16, that the stagnating shell can lose almost half of its radial kinetic energy or margin for every 100 ps traveled. As a result, there exists a critical timing involving the onset of ignition and the decreasing margin in the shell. If ignition is delayed beyond the time at which the point design would normally ignite ($t = 0$ in Fig. 84.16), the shell's margin drops and the final gain is diminished. If ignition is delayed too long, the shell will stagnate, the PdV work will cease, and the implosion will fail. Recalling that the margin for the gain threshold is roughly 10%, the high-gain window for this target, as shown in Fig. 84.16, is ~120 ps.

One of the roles of increasing perturbations at the ice/vapor interface is to delay the onset of ignition. As was pointed out by Levedahl and Lindl[37] and Kishony,[22] one can view increasing perturbation amplitudes as being an equivalent reduction in implosion velocity. The increased surface area and perturbed volume of the hot spot allow for an increase in the thermal

conduction losses and a decrease in the absorbed energy density of α particles within the hot spot. To reach ignition requires that the hot spot be driven to a higher ρR to recoup these losses. A high-gain shell, by our definition, still has excess kinetic energy to complete the task; however, this delays ignition and depletes the shell of valuable margin. The results of *ORCHID* simulations clearly show, as displayed in Fig. 84.17(a), how increasing $\bar{\sigma}$ affects ignition timing and the margin of the implosion. The point design resides in a linear, albeit steep, region of the ignition cliff. One should then expect a linear response of the burn-up fraction (i.e., gain) to changes in implosion margin. Such a linear behavior is clearly indicated in Fig. 84.17(b), where the calculated gains from the *ORCHID* simulations are drawn as a function of their calculated margin. The argument of increasing shell nonuniformities effectively depleting the shell margin explains the performance of targets giving intermediate gains for intermediate values of $\bar{\sigma}$.

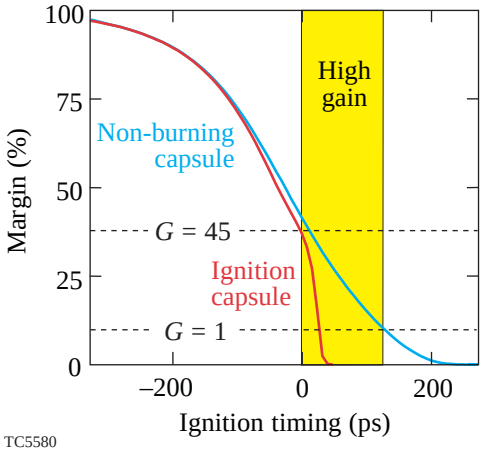

Figure 84.16
Shell stagnation determines the margin trajectory, which, in turn, defines the window for high gain.

Uniformity Budget for NIF

A global nonuniformity budget for the direct-drive point design on NIF can now be constructed in terms of $\bar{\sigma}$. If each of the four sources of nonuniformity acts independently, then the total effect can be measured by adding the individual $\bar{\sigma}$'s in quadrature $\bar{\sigma}_t$. Figure 84.18 displays the dependence of $\bar{\sigma}$ for each of the four main sources as a function of their individual laser and target specifications. Specification values have been scaled to reflect a universal multiplier that serves as the y axis. The sum-in-quadrature value $\bar{\sigma}_t = 1.4$ for this system (using current NIF specifications with two color cycles) is plotted as the solid dot on the inset graph of gain versus $\bar{\sigma}_t$ and represents a capsule gain of slightly greater than 30. The largest contributor can be seen to be the effects of laser nonuniformity. While the on-target power imbalance also makes a strong contribution, the effects due to the roughness of the ice/vapor interface are manageable and those due to outer-surface roughness are of no real consequence. If the NIF specifications of two color cycles are not achieved and only one color cycle is used, then the combined $\bar{\sigma}_t$ increases from 1.4 to 1.75, as seen in Fig. 84.10. The resultant target gain drops from 30 to 20. At one color cycle, the gain could be brought back to 30 by

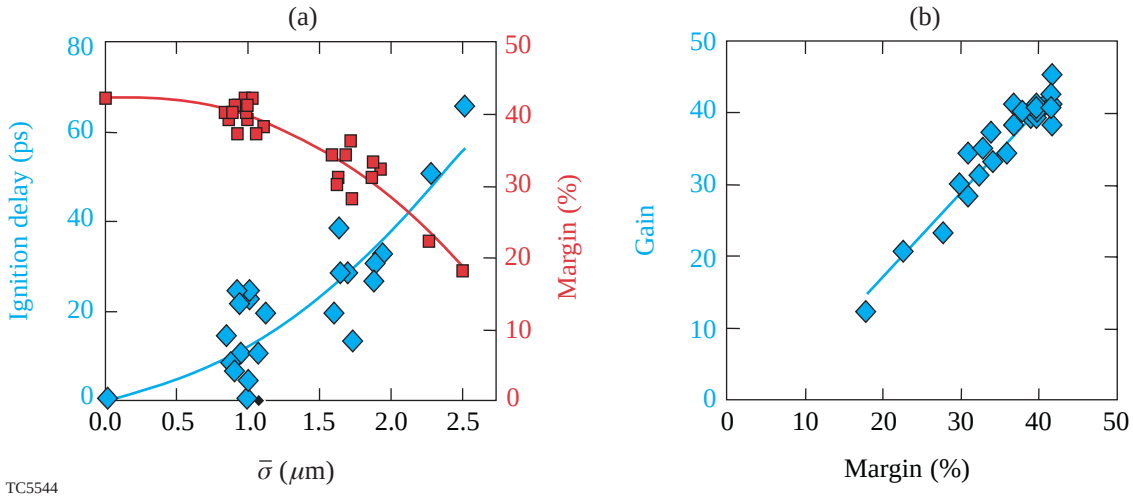

Figure 84.17
ORCHID simulations indicate that hot-spot ignition is delayed as ice/vapor interface perturbations increase. (a) Increasing shell perturbations ($\bar{\sigma}$) act to increase ignition delay (◆). This delay causes the burn wave to sample a shell with decreased margin (■). (b) Capsule gain depends strongly on the shell margin at ignition.

doubling the bandwidth, but this has been precluded by the efficiency of the frequency-tripling crystals. The achievement of two color cycles is consistent with current-day technology, but propagation issues through the laser chain must still be examined. At the two-color-cycle level, even higher gains can be achieved with improvements in power-balance technology.

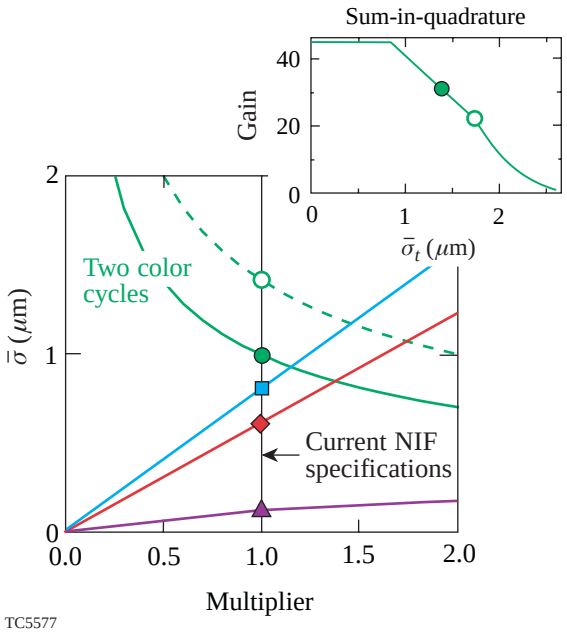

Figure 84.18
ORCHID results can be used to scale the target gain with $\bar{\sigma}$ to form a global nonuniformity budget for the direct-design point design. The *y* axis scales to the parameters: SSD bandwidth, one color cycle (○, × 1 THz); SSD bandwidth, two color cycles (●, × 1 THz); on-target power imbalance (■, × 2% rms); inner ice roughness (◆, × 1 μm rms); and outer-surface roughness (▲, × 80 nm).

Conclusions

Capsule gain can be directly related to the kinetic energy of the incoming shell that is in excess of the energy required to achieve ignition. When related to the peak kinetic energy of the implosion, this excess kinetic energy can be cast in terms of an implosion margin. Shell margin, prior to ignition, depends only on the temporal stagnation of the shell. As such, high gain requires the onset of ignition to coincide with significant (~40%) retained shell margin. Our analysis indicates that increasing perturbations in the incoming shell delay the onset of ignition within the hot spot. During this delay, the shell continues to stagnate and lose valuable margin. When ignition does occur, the burn wave samples the depleted shell margin allowing the high ignition pressure to decompress the main fuel layer prematurely, which leads to reduced gain. If the perturbations of the incoming shell delay ignition too long, the shell will stagnate, the PdV work will cease, and the implosion will fail.

The two-dimensional hydrodynamics code *ORCHID* has been used to examine the target performance of the NIF direct-drive point design driven under the influence of the four main sources of nonuniformity: laser imprint, power imbalance, and inner- and outer-target-surface roughness. Results from these studies indicate that capsule gain can be scaled to the rms spectrum of the ice/vapor surface deformation at the end of the acceleration stage of the implosion. Applying this scaling shows that NIF direct-drive point design performance is most sensitive to the effects of SSD smoothing, followed by power imbalance, inner-ice-surface roughness, and outer-surface roughness. A global nonuniformity budget was constructed using the scaling of a varied set of *ORCHID* simulations to evaluate the net effect of all nonuniformities acting together. This budget indicates that, if laser smoothing, power imbalance, and both inner- and outer-surface roughness stay within the limits specified by NIF direct-drive requirements, the capsule shell remains intact during the implosion and the implosion results in $G \sim 30$.

REFERENCES

1. M. D. Campbell and W. J. Hogan, Plasma Phys. Control. Fusion **41**, B39 (1999).
2. J. D. Lindl, Phys. Plasmas **2**, 3933 (1995).
3. Laboratory for Laser Energetics LLE Review **79**, 121, NTIS document No. DOE/SF/19460-317 (1999). Copies may be obtained from the National Technical Information Service, Springfield, VA 22161.
4. Lord Rayleigh, in *Scientific Papers* (Cambridge University Press, Cambridge, England, 1900), Vol. II, pp. 200–207.
5. M. S. Plesset, J. Appl. Phys. **25**, 96 (1954); G. I. Bell, Los Alamos National Laboratory, Report No. LA-1321 (1951).
6. S. E. Bodner, D. G. Colombant, J. H. Gardner, R. H. Lehmberg, S. P. Obenschain, L. Phillips, A. J. Schmitt, J. D. Sethian, R. L. McCrory, W. Seka, C. P. Verdon, J. P. Knauer, B. B. Afeyan, and H. T. Powell, Phys. Plasmas **5**, 1901 (1998).
7. S. W. Haan *et al.*, Phys. Plasmas **2**, 2480 (1995).
8. M. M. Marinak *et al.*, Phys. Plasmas **5**, 1125 (1998).
9. T. R. Dittrich *et al.*, Phys. Plasmas **5**, 3708 (1998).
10. S. V. Weber, S. G. Glendinning, D. H. Kalantar, M. H. Key, B. A. Remington, J. E. Rothenberg, E. Wolfrum, C. P. Verdon, and J. P. Knauer, Phys. Plasmas **4**, 1978 (1997).

11. V. N. Goncharov, S. Skupsky, P. W. McKenty, J. A. Delettrez, R. P. J. Town, and C. Cherfils-Clérouin, in *Inertial Fusion Sciences and Applications 99*, edited by C. Labaune, W. J. Hogan, and K. A. Tanaka (Elsevier, Paris, 2000), pp. 214–219.

12. R. Betti, V. Lobatchev, and R. L. McCrory, Phys. Rev. Lett. **81**, 5560 (1998).

13. D. P. Smitherman *et al.*, Phys. Plasmas **6**, 932 (1999).

14. K. Shigemori *et al.*, Phys. Rev. Lett. **84**, 5331 (2000).

15. C. P. Verdon, Bull. Am. Phys. Soc. **38**, 2010 (1993).

16. M. C. Richardson, P. W. McKenty, F. J. Marshall, C. P. Verdon, J. M. Soures, R. L. McCrory, O. Barnouin, R. S. Craxton, J. Delettrez, R. L. Hutchison, P. A. Jaanimagi, R. Keck, T. Kessler, H. Kim, S. A. Letzring, D. M. Roback, W. Seka, S. Skupsky, B. Yaakobi, S. M. Lane, and S. Prussin, in *Laser Interaction and Related Plasma Phenomena*, edited by H. Hora and G. H. Miley (Plenum Publishing, New York, 1986), Vol. 7, pp. 421–448.

17. R. L. McCrory and C. P. Verdon, in *Inertial Confinement Fusion*, edited by A. Caruso and E. Sindoni (Editrice Compositori, Bologna, Italy, 1989), pp. 83–124.

18. V. N. Goncharov, Phys. Rev. Lett. **82**, 2091 (1999); R. Ishizaki and K. Nishihara, Phys. Rev. Lett. **78**, 1920 (1997); R. J. Taylor *et al.*, Phys. Rev. Lett. **79**, 1861 (1997); A. L. Velikovich *et al.*, Phys. Plasmas **5**, 1491 (1998).

19. S. P. Obenschain *et al.*, Phys. Rev. Lett. **46**, 1402 (1981); S. G. Glendinning, S. N. Dixit, B. A. Hammel, D. H. Kalantar, M. H. Key, J. D. Kilkenny, J. P. Knauer, D. M. Pennington, B. A. Remington, R. J. Wallace, and S. V. Weber, Phys. Rev. E **54**, 4473 (1996); R. J. Taylor *et al.*, Phys. Rev. Lett. **76**, 1643 (1996); C. J. Pawley *et al.*, Phys. Plasmas **4**, 1969 (1997); V. A. Smalyuk, T. R. Boehly, D. K. Bradley, V. N. Goncharov, J. A. Delettrez, J. P. Knauer, D. D. Meyerhofer, D. Oron, D. Shvarts, Y. Srebro, and R. P. J. Town, Phys. Plasmas **6**, 4022 (1999).

20. V. N. Goncharov, S. Skupsky, T. R. Boehly, J. P. Knauer, P. McKenty, V. A. Smalyuk, R. P. J. Town, O. V. Gotchev, R. Betti, and D. D. Meyerhofer, Phys. Plasmas **7**, 2062 (2000).

21. Laboratory for Laser Energetics LLE Review **23**, 125, NTIS document No. DOE/SP40200-03 (1985). Copies may be obtained from the National Technical Information Service, Springfield, VA 22161.

22. R. Kishony, "Ignition Criterion in Inertial Confinement Fusion Using Self-Similar Solutions, and the Effect of Perturbations on Ignition," Ph.D. thesis, Tel Aviv University, 1999.

23. J. D. Lindl, *Inertial Confinement Fusion: The Quest for Ignition and Energy Gain Using Indirect Drive* (Springer-Verlag, New York, 1998), p. 3.

24. V. Lobatchev and R. Betti, "Ablative Stabilization of the Deceleration-Phase Rayleigh-Taylor Instability," to be published in Physical Review Letters.

25. O. S. Jones, Lawrence Livermore National Laboratory, private communication (2000).

26. O. S. Jones *et al.*, in *NIF Laser System Performance Ratings*, Supplement to Third Annual International Conference on Solid State Lasers for Application to Inertial Confinement Fusion (SPIE, Bellingham, WA, 1998), Vol. 3492, pp. 49–54.

27. V. N. Goncharov, P. McKenty, S. Skupsky, R. Betti, R. L. McCrory, and C. Cherfils-Clérouin, "Modeling Hydrodynamic Instabilities in Inertial Confinement Fusion Targets," to be published in Physics of Plasmas.

28. T. R. Boehly, V. N. Goncharov, O. Gotchev, J. P. Knauer, D. D. Meyerhofer, D. Oron, S. P. Regan, Y. Srebro, W. Seka, D. Shvarts, S. Skupsky, and V. A. Smalyuk, "Optical and Plasma Smoothing of Laser Imprinting in Targets Driven by Lasers with SSD Bandwidths Up to 1 THz," to be published in Physics of Plasmas.

29. Y. Kato *et al.*, Phys. Rev. Lett. **53**, 1057 (1984).

30. Laboratory for Laser Energetics LLE Review **33**, 1, NTIS document No. DOE/DP/40200-65 (1987). Copies may be obtained from the National Technical Information Service, Springfield, VA 22161.

31. T. R. Boehly, V. A. Smalyuk, D. D. Meyerhofer, J. P. Knauer, D. K. Bradley, R. S. Craxton, M. J. Guardalben, S. Skupsky, and T. J. Kessler, J. Appl. Phys. **85**, 3444 (1999).

32. Laboratory for Laser Energetics LLE Review **36**, 158, NTIS document No. DOE/DP/40200-79 (1988). Copies may be obtained from the National Technical Information Service, Springfield, VA 22161.

33. R. Epstein, J. Appl. Phys. **82**, 2123 (1997).

34. S. Skupsky and R. S. Craxton, Phys. Plasmas **6**, 2157 (1999).

35. R. H. Lehmberg, A. J. Schmitt, and S. E. Bodner, J. Appl. Phys. **62**, 2680 (1987).

36. W. K. Levedahl and J. D. Lindl, Nucl. Fusion **37**, 165 (1997).

37. *ibid.*, p. 171.